AGU PUBLICATIONS

JGR

Journal of Geophysical Research: Atmospheres

RESEARCH ARTICLE

10.1002/2014JD022895

Key Points:

- A LDAS is developed to improve the skill of an ecohydrological model
- Microwave data assimilation can improve 0–15 cm depth soil moisture simulation

Supporting Information:

- Figures S1–S3

Correspondence to:
Y. Sawada,
yoheisawada@hydra.t.u-tokyo.ac.jp

Citation:
Sawada, Y., T. Koike, and J. P. Walker (2015), A land data assimilation system for simultaneous simulation of soil moisture and vegetation dynamics, *J. Geophys. Res. Atmos.*, *120*, 5910–5930, doi:10.1002/2014JD022895.

Received 26 NOV 2014
Accepted 31 MAY 2015
Accepted article online 3 JUN 2015
Published online 29 JUN 2015

A land data assimilation system for simultaneous simulation of soil moisture and vegetation dynamics

Yohei Sawada[1], Toshio Koike[1], and Jeffrey P. Walker[2]

[1]Department of Civil Engineering, School of Engineering, The University of Tokyo, Bunkyo-ku, Tokyo, Japan, [2]Department of Civil Engineering, Monash University, Clayton, Australia

Abstract Despite the importance of the coupling between vegetation dynamics and root-zone soil moisture in land-atmosphere interactions, there is no land data assimilation system (LDAS) that currently addresses this issue, limiting the capacity to positively impact weather and seasonal forecasting. We develop a new LDAS that can improve the skill of an ecohydrological model to simulate simultaneously surface soil moisture, root-zone soil moisture, and vegetation dynamics by assimilating passive microwave observations that are sensitive to both surface soil moisture and terrestrial biomass. This LDAS first calibrates both hydrological and ecological parameters of a land surface model, which explicitly simulates vegetation growth and senescence. Then, it adjusts the model states of soil moisture and leaf area index (LAI) sequentially using a genetic particle filter. We can adjust the subsurface soil moisture, which is not observed directly by satellites, because we simulate the interactions between vegetation dynamics and subsurface water dynamics. From a point-scale evaluation, we succeed in improving the performance of our land surface model and generate ensembles of the model state whose distribution reflects the combined information in the land surface model and satellite observations. We show that the adjustment of the subsurface soil moisture significantly improves the capacity to simulate vegetation dynamics in seasonal forecast timescales. This LDAS can contribute to the generation of ensemble initial conditions of surface and subsurface soil moisture and LAI for a probabilistic framework of weather and seasonal forecasting.

1. Introduction

Land surface conditions are an important factor in weather and seasonal prediction. Soil moisture and terrestrial biomass affect the energy partitioning of the land surface by regulating the albedo and Bowen ratio [e.g., *Samain et al.*, 2008; *Timouk et al.*, 2009]. Moreover, the representation of land-atmosphere interactions in numerical simulations strongly governs the skill of regional-scale weather forecasting [e.g., *Hohenegger et al.*, 2009; *Garcia-Carreras and Parker*, 2011; *Zaitchik et al.*, 2013]. *Yuan and Wood* [2013] have shown that 3 month seasonal predictions have limited skill in forecasting the onset of global drought at local scales and that local land-atmosphere coupling, in addition to the coupling between sea surface temperature and drought, needs to be investigated to improve this skill. To estimate soil moisture and terrestrial biomass impact on the land surface feedbacks to the atmosphere and improve the representation of land-atmosphere interactions in the land-ocean-atmosphere forecasting system, many land surface models (LSMs) have been developed [e.g., *Clark et al.*, 2011; *Lawrence et al.*, 2011; *Yang et al.*, 2011; *Boussetta et al.*, 2013].

A land data assimilation system (LDAS) can effectively combine information from an LSM with observations and is a promising technique by which to improve LSM-based land surface forecasting [*Montzka et al.*, 2012]. While the number of in situ observations is insufficient to address the heterogeneities of land surface conditions, satellite observations make it possible to globally assimilate observed data into an LSM. In particular, the application of satellite-based passive microwave remote sensing observations to an LDAS has been intensively investigated for improving the skill of soil moisture forecast through assimilation [e.g., *Yang et al.*, 2007, 2009; *Qin et al.*, 2009; *Tian et al.*, 2009; *Li et al.*, 2012a; *Su et al.*, 2013]. This is because surface soil moisture can be retrieved well from the microwave brightness temperature observations [e.g., *Paloscia et al.*, 2001; *Njoku et al.*, 2003; *Gruhier et al.*, 2008; *Owe et al.*, 2008; *Jackson et al.*, 2010; *Albergel et al.*, 2012]. Coupling of a microwave radiative transfer, land surface model, and atmospheric model with a data assimilation system has already been realized [*Rasmy et al.*, 2011].

In addition, there have been many other contributions to LDASs to improve the simulation of water cycle components on land. For example, *Li et al.* [2012b] evaluated the potential of terrestrial water storage assimilation from the Gravity Recovery and Climate Experiment (GRACE) into an LSM to improve the simulation of groundwater and runoff. *Zhang et al*. [2014] have shown that the assimilation of snow-cover fraction from the Moderate Resolution Imaging Spectroradiometer (MODIS) improved the simulation of snow water equivalent and snow depth considerably.

However, previous developments have focused mainly on the water cycle components of the land system and have omitted to explicitly simulate the interactions between the water cycle and vegetation dynamics. For correct simulation of the vegetation condition, the coupling of subsurface soil moisture and vegetation dynamics is important. For example, *Sanchez-Mejia and Papuga* [2014] and *Sanchez-Mejia et al*. [2014] have provided observational evidence that the dynamics of subsurface soil moisture strongly regulates the canopy albedo and evaporative fraction. These observations highlight the importance of the coupling between subsurface soil moisture and vegetation dynamics in land-atmosphere interactions. To forecast this coupling, it is necessary to obtain simultaneously the initial conditions of the root-zone soil moisture vertical profile and the terrestrial biomass.

The joint assimilation of surface soil moisture and leaf area index (LAI) has been realized by *Sabater et al*. [2008], which introduced in situ observation into the ISBA-A-g_s LSM. *Sabater et al*. [2008] investigated how to improve root-zone soil moisture simulation by assimilating only land surface information [see also *Albergel et al*., 2010; *Bardu et al*., 2011]. *Nearing et al*. [2012] assessed the impact of LAI and soil moisture assimilation for wheat yield estimates by an observing system simulation experiment and concluded this joint assimilation has the limited capacity to improve yield estimates due mainly to a lack of root-zone soil moisture information. Since it is difficult to directly obtain information of subsurface soil moisture from space, how to propagate the land surface observation to deeper soil layers has been deeply discussed.

As a globally applicable satellite product, the visible-infrared MODIS LAI has been frequently used to improve the simulation of vegetation phenology. *Jarlan et al*. [2008] have described a LAI data assimilation system using MODIS LAI and Carbon-TESSEL LSM. *Stöckli et al*. [2008] and *Stöckli et al*. [2011] have realized a global long-term reanalysis of vegetation phenology by assimilating MODIS LAI and a fraction of photosynthetically active radiation into the simple phenology model. However, these studies did not discuss the simulation of surface and subsurface soil moisture. A satellite-based LDAS that can simultaneously improve the simulation of soil moisture and vegetation dynamics has yet to be developed.

Vegetation dynamics can also be retrieved from the microwave brightness temperature [e.g., *Paloscia and Pampaloni*, 1988; *Owe et al*., 2001; *Jones et al*., 2011; *Liu et al*., 2011]. Therefore, passive microwave remote sensing also has the capacity to improve the simulation of vegetation dynamics using data assimilation techniques, thus mitigating the need to rely upon cloud-limited optical data. *Sawada and Koike* [2014a, 2014b] have demonstrated that it is possible to simultaneously calibrate hydrological and ecological parameters in an ecohydrological model using passive microwave satellite observations and improve the skill of simulating both soil moisture and LAI.

The aim of this paper is to develop an LDAS that can generate an ensemble initial surface soil moisture, subsurface soil moisture, and terrestrial biomass conditions for probabilistic forecasting [e.g., *Wood and Lettenmaier*, 2008; *Pan et al*., 2013; *Yuan and Wood*, 2013] by assimilating passive microwave satellite observations. This LDAS, a Coupled Land and Vegetation Data Assimilation System (CLVDAS), has an LSM coupled with a dynamic vegetation model (DVM) to calculate vegetation growth and senescence, and a radiative transfer model (RTM) to predict emission in the microwave region. First, the CLVDAS optimizes both hydrological and ecological model parameters simultaneously by comparing modeled and observed microwave brightness temperatures. Second, the CLVDAS adjusts the model state of surface soil moisture, subsurface soil moisture, and LAI at the same time by assimilating satellite-observed brightness temperatures using genetic particle filtering (GPF). We can adjust the subsurface soil moisture by assimilating satellite vegetation observations because we explicitly model the interactions between subsurface soil moisture and vegetation dynamics. *Sawada and Koike* [2014a, 2014b] have already described and tested the parameter optimization part of the CLVDAS. Thus, in this paper, we focus on the capability of GPF to adjust the model state to generate ensemble initial conditions by assimilating Advanced Microwave Scanning Radiometer 2 (AMSR2)-observed brightness temperatures.

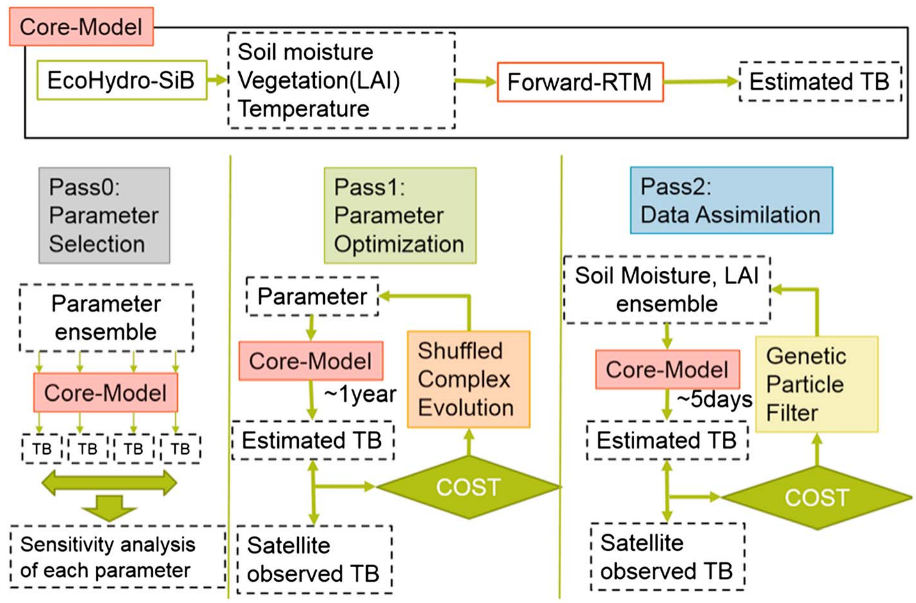

Figure 1. Structure of the coupled land and vegetation data assimilation system (CLVDAS).

2. Coupled Land and Vegetation Data Assimilation System

Figure 1 shows the CLVDAS structure. EcoHydro-SiB calculates the surface soil moisture, LAI, surface temperature, and canopy temperature, which are fed into the RTM to estimate brightness temperatures (TB in Figure 1) in the microwave region. We defined this model chain as the Core-Model in Figure 1.

The CLVDAS has three different modules: parameter selection, parameter optimization, and data assimilation. First, we analyze the parameter sensitivities of EcoHydro-SiB using a global sensitivity analysis approach to reduce the number of optimized parameters. Second, the parameter optimization module estimates the hydrological and ecological parameters by fitting estimated brightness temperatures to the observed brightness temperatures. Third, in the data assimilation module, we adjust the vertical soil moisture profile and LAI using GPF.

In the first two modules (Pass0 and Pass1 in Figure 1), a long time window was chosen (1 year in this study) because model parameters do not change in a short period of time, whereas in the third module (Pass2 in Figure 1), a shorter time window (5 days in this study) was used because initial conditions of soil moisture and LAI have a short-term effect on the system state variables [see also *Yang et al.*, 2009]. The dual-pass data assimilation, which uses the observation data in the two different passes (parameter optimization and model state adjustment), has already been implemented in the previous microwave LDAS studies [*Yang et al.*, 2007, 2009; *Tian et al.*, 2009]. *Vrugt et al.* [2013] pointed out that if both the model parameters and state variables are simultaneously adjusted in the single short time window, the posterior distributions of model parameters can change considerably through time due to temporal changes in parameter sensitivity. To obtain time-invariant single optimized parameters, the dual-pass data assimilation has been chosen as the algorithm for the CLVDAS.

In this section, we describe the models (EcoHydro-SiB and RTM) and these three modules. As *Sawada and Koike* [2014b] have already presented an explanation of the CLVDAS, except for the GPF data assimilation part, we mainly describe the new modules (Pass2 in Figure 1) and modifications from the version of *Sawada and Koike* [2014b] in this paper. Please see the detailed explanation and complete formulations in *Sawada and Koike* [2014b], although a brief description is presented in this paper.

2.1. Land Surface Model: EcoHydro-SiB

EcoHydro-SiB is the LSM of the CLVDAS. This model was originally the coupled model of Hydro-SiB and DVM. Hydro-SiB was developed by *Wang et al.* [2009c] by improving the hydrology of the Simple Biosphere Model 2 [*Sellers et al.*, 1996]. Many studies have evaluated Hydro-SiB within the framework of a distributed hydrological model [e.g., *Wang et al*., 2009a, 2009b, 2009c, 2011; *Saavedra et al*., 2010; *Jaranilla-Sanchez et al*., 2011; *Xue et al*., 2013].

In Hydro-SiB, the vertical interlayer flows within the unsaturated zone are described using a one-dimensional Richards's equation. In *Sawada and Koike* [2014b], the capillary suction and hydraulic conductivity are calculated by van Genuchten's water retention curve [*van Genuchten*, 1980]. However, in this paper, we calculate capillary suction using the modified van Genuchten model, as suggested by *Ciocca et al*. [2014], to describe the water dynamics of dry soil, but with the original van Genuchten's equations to calculate the hydraulic conductivity. The formulations are as follows:

$$\psi(\theta) = \frac{1}{\alpha}\left(S_{\mathrm{MVG}}{}^{1/m^*}\right)^{1/n^*}, \tag{1}$$

$$K(\theta,z)/K_s(z) = S^{1/2}\left[1-\left(1-S^{1/m}\right)^m\right]^2, \tag{2}$$

$$S = (\theta-\theta_r)/(\theta_s-\theta_r), \tag{3}$$

$$S_{\mathrm{MVG}} = \theta/\theta_s \tag{4}$$

$$m = 1-1/n,\ \ m^* = 1-1/n^*, \tag{5}$$

where z is the distance from the surface with positive values increasing vertically downwards (m), θ is the volumetric water content (m^3/m^3), $\psi(\theta)$ is the capillary suction (m), $K(\theta,z)$ is the hydraulic conductivity (m/s), $K_s(z)$ is the saturated hydraulic conductivity (m/s), θ_r is the residual water content (m^3/m^3), θ_s is the saturation water content or porosity (m^3/m^3), and α, n, and n^* are model parameters. In the original formulations of *van Genuchten* [1980], S was used for calculating capillary suction, but it is replaced with S_{MVG} here. In the CLVDAS, we firstly specify parameters α and n and then calculate n^* by fitting our water retention curve to the original van Genuchten's water retention curve under wet conditions ($\theta > 0.1$) [see also *Ciocca et al*., 2014].

We assume the saturated hydraulic conductivity decreases exponentially with increasing soil depth [*Cabral et al*., 1992; *Robinson and Sivapalan*, 1996]:

$$K_s(z) = K_s(0)\exp(-fz), \tag{6}$$

where f is the decay factor. This assumption is derived by a number of field studies [*Beven*, 1982]. A detailed explanation of the hydrology of Hydro-SiB can be found in *Wang et al*. [2009c].

We have developed the DVM to be coupled with Hydro-SiB (EcoHydro-SiB). The capability of estimating water cycle and vegetation dynamics has been evaluated within the framework of the distributed hydrological model [*Sawada and Koike*, 2013; *Sawada et al*., 2014]. In the grassland case, carbon-pool dynamics are modeled by the following equations:

$$\frac{\mathrm{d}C_{\mathrm{leaf}}}{\mathrm{d}t} = a_{\mathrm{leaf}}\mathrm{NPP} - (d_{\mathrm{leaf}}+\gamma+\lambda)C_{\mathrm{leaf}} \tag{7}$$

$$\frac{\mathrm{d}C_{\mathrm{root}}}{\mathrm{d}t} = a_{\mathrm{root}}\mathrm{NPP} - d_{\mathrm{root}}C_{\mathrm{root}}, \tag{8}$$

where C_{leaf} and C_{root} are the carbon pools of leaves and roots, respectively [kg/m^2], a_{leaf} and a_{root} are the carbon allocation fractions of leaves and roots, respectively, and $a_{\mathrm{leaf}}+a_{\mathrm{root}}=1$. NPP is the net primary production ($mol/m^2/s$), d_{leaf} and d_{root} are the normal turnover rates of leaves and roots, respectively, and γ and λ are water- and temperature-related stress factors for leaves, respectively. In the woody biomass case, we consider the sapwood carbon pool.

A water-related stress factor is derived from the vertical distribution of soil moisture, following the method of *Arora and Boer* [2005] using a soil moisture index (SMI):

$$\beta_T(i) = \min\left[1, \max\left(0, \frac{\theta_i-\theta_w}{\theta_o-\theta_w}\right)\right], \tag{9}$$

where $\beta_T(i)$ is the SMI of the i-th soil layer, θ_i is the volumetric soil moisture, θ_w is the wilting point, and θ_o is the point of stress onset. To obtain θ_w and θ_o, we specify the corresponding suction value and inversely solve equations (1) and (4). β_{TOT} is calculated by aggregating the SMI in the root-zone layers, weighted by the root biomass fraction, as in the model of *Jackson et al*. [1996].

$$Y(d) = 1 - B^d \tag{10}$$

where Y is the cumulative root fraction from the surface to depth d (cm) and B is an empirical parameter that is <1. Thus, β_{TOT} is calculated by

$$\beta_{TOT} = \sum_{i=1}^{N} \beta_T(i)\times[Y(\Delta z_i \times i) - Y(\Delta z_i \times (i-1))], \tag{11}$$

where N is the number of soil layers and Δz_i is the depth of each. This method was used in *Ivanov et al*. [2008]. Water-related stress factor γ in our DVM is defined by

$$\gamma = \gamma_{max}(1 - \beta_{TOT})^4, \tag{12}$$

where γ_{max} is the maximum stress loss. The methodology to calculate other factors in equations (6) and (7) can be found in *Sawada and Koike* [2014b] and *Sawada et al*. [2014].

Once we have estimated a carbon pool of leaves, the LAI and vegetation water content (VWC) can be obtained using the empirical relationships proposed by *Calvet et al*. [1998] and *Paloscia and Pampaloni* [1988]:

$$\mathrm{LAI} = \mathrm{SLA} \times C_{leaf}, \tag{13}$$

$$\mathrm{VWC} = \exp(\mathrm{LAI}/3.3) - 1, \tag{14}$$

where SLA is the specific leaf area that indicates leaf thickness (m^2/kg) [see *Arora and Boer*, 2005] and VWC is one of the input variables of the RTM.

The time step of the model was set to 1 h, and the thicknesses of the soil layers were set to 5 cm. The root-zone soil is arbitrary defined as the soil layer 5–95 cm from the surface. However, please note that the root biomass is not uniformly distributed in the root-zone soil of EcoHydro-SiB [see equation (10)]. Soil moisture-vegetation coupling in shallower layers is therefore much stronger than that in deeper layers (see also section 3.1). The total soil thickness was set to 150 cm.

2.2. Radiative Transfer Model

Because we directly assimilate brightness temperatures into the model instead of derived soil moisture and vegetation products, we need to have an RTM to convert the land surface conditions to microwave brightness temperatures. The inputs of the RTM are surface soil moisture, surface temperature, canopy temperature, and the VWC calculated by EcoHydro-SiB. The total emission and attenuation from the land surface and vegetation canopy can be calculated using the equation [*Mo et al*., 1982]:

$$T_b = T_{bs}\exp(-\tau_c) + (1-\omega_c)T_c(1-\exp(-\tau_c)) + R_p(1-\omega_c)T_c(1-\exp(-\tau_c))\exp(-\tau_c) \tag{15}$$

where T_b is the brightness temperature at radiometer level, T_{bs} is the brightness temperature at ground level $T_{bs} = (1 - R_p)T_s$, T_s and T_c are the physical land surface and canopy temperatures, respectively, ω_c is the single scattering albedo of the canopy, R_p is the reflectivity of the land surface, and subscript p indicates the polarization (vertical or horizontal). τ_c is the vegetation optical depth (VOD), which is calculated using

$$\tau_c = \frac{b' {\lambda_c}^x \mathrm{VWC}}{\cos\theta}, \tag{16}$$

where b' is the vegetation parameter that is independent of wavelength (λ_c), x is a parameter that shows a dependence on wavelength (in shorter wavelength, microwave is easier to be attenuated by the vegetation water content), and θ is the incident angle. Equation (16) was proposed by *Jackson and Schmugge* [1991].

Calculating land surface emissivity ($=1-R_p$) is the important part of the RTM. In the CLVDAS, we use an Advanced Integral Equation Model with the incorporation of a shadowing effect [*Kuria et al.*, 2007]. This model is suitable for describing surface emission and surface scattering for a wide range of surface roughness conditions characterized by rms height (hmv) and correlation length (Qmv). *Kuria et al.* [2007] validated this RTM through field experiments. The formulations of this model can be found in *Kuria et al.* [2007] and *Sawada and Koike* [2014b].

2.3. Parameter Selection Strategy

Although the model has a large number of unknown parameters, we can calibrate simultaneously a limited number of them by considering the efficiency of the optimization computation. Therefore, the CLVDAS realizes the parameter sensitivity analysis to select those parameters to be calibrated (Pass0 in Figure 1). We perform a variance-based global sensitivity analysis [*Qin et al.*, 2009; *Saltelli et al.*, 2010; *Marzban*, 2013; *Pappas et al.*, 2013] for several parameters of EcoHydro-SiB. The total sensitivity index, which measures the sum of all the effects related to a parameter [*Qin et al.*, 2009], is calculated, and we select those parameters sensitive to the model-estimated brightness temperatures at the scan time of a microwave radiometer as the calibrated parameters (the list of selected parameters in this study can be found in section 4). The details of this technique can be found in *Sawada and Koike* [2014b].

2.4. Parameter Optimization

The parameter optimization module of the CLVDAS (Pass1 in Figure 1) searches the optimized parameters by minimizing the cost function:

$$\mathrm{COST}=\sum_{t=0}^{t=T}\begin{bmatrix}\left(T_{\mathrm{b,est}}^{6.9\mathrm{V}}-T_{\mathrm{b,obs}}^{6.9\mathrm{V}}\right)^2+\left(T_{\mathrm{b,est}}^{6.9\mathrm{H}}-T_{\mathrm{b,obs}}^{6.9\mathrm{H}}\right)^2+\left(T_{\mathrm{b,est}}^{10.7\mathrm{V}}-T_{\mathrm{b,obs}}^{10.7\mathrm{V}}\right)^2\\+\left(T_{\mathrm{b,est}}^{10.7\mathrm{H}}-T_{\mathrm{b,obs}}^{10.7\mathrm{H}}\right)^2+\left(T_{\mathrm{b,est}}^{18.7\mathrm{V}}-T_{\mathrm{b,obs}}^{18.7\mathrm{V}}\right)^2+\left(T_{\mathrm{b,est}}^{18.7\mathrm{H}}-T_{\mathrm{b,obs}}^{18.7\mathrm{H}}\right)^2\end{bmatrix}, \tag{17}$$

where the subscript obs denotes the observed value and est denotes the model's estimated value. We assimilate the observed brightness temperatures (T_b) of the vertical (V) and horizontal (H) polarization at 6.9, 10.7, and 18.7 GHz frequencies, using the summation of square errors during a calibration period (T, 1 year in this study). This cost function differs slightly from that of *Sawada and Koike* [2014b], which assimilated brightness temperatures at only 6.9 and 18.7 GHz. Here we used three different frequencies because it makes the system more stable, especially when we adjust the model state directly (see section 2.5), although the computational costs do increase.

As discussed in *Sawada and Koike* [2014b], we identify the initial guess of the targeted parameters by referring to the map of global soil texture and land use type in each grid to confirm the physical consistency among the parameter values. Then, we add the uncertainty to this initial guess as the upper and lower bounds of the optimized parameters considering a reasonable range. The CLVDAS finds the optimal parameters that minimize the cost function [equation (17)] by using the shuffled complex evolution method (SCE-UA) [*Duan et al.*, 1992].

2.5. Data Assimilation: Genetic Particle Filter

We chose the particle filtering (PF) approach to sequentially adjust the model state in the CLVDAS (Pass2 in Figure 1). In comparison with the Kalman Filter (KF), including the Ensemble Kalman Filter, the advantage of PF is that the posterior distribution of the state vector can be represented by Monte Carlo samples and the Gaussian assumption is eliminated [*Qin et al.*, 2009]. In addition, PF is more robust than KF against model nonlinearity. Although the disadvantage of PF is its high computational cost, it is feasible to apply PF to an LDAS whose numerical models (one-dimensional LSMs) do not greatly consume computational resources.

The theoretical background, algorithm, and application of GPF can be found in *Mechri et al.* [2014], *Rémy et al.* [2012], *Kwok and Zhou* [2005], and *Uosaki et al.* [2004]. The procedure of GPF can be divided into three steps: selection, resample, and mutation. We define the model vectors at time t as $x_{t,i}(i=1,2,\dots\dots,N)$, where i denotes the subscript of the Monte Carlo samples (hereafter called "particles") and N is the total number of particles. In the CLVDAS, each model vector has a value of soil moisture in each surface and root-zone layer, and the LAI, such that

$$x_{t,i} = \begin{bmatrix} \theta_1 \\ \theta_2 \\ \theta_3 \\ . \\ . \\ . \\ . \\ \theta_{\mathrm{rn}} \\ \mathrm{LAI} \end{bmatrix}, \tag{18}$$

where θ_n is the n-th soil moisture layer and rn (=20 in this study) is the total number of soil layers from the top of the soil to the bottom of the root zone.

The total number of particles needs to be selected carefully to avoid filter collapse [*Mechri et al.*, 2014; *Rémy et al.*, 2012]. In this paper, we set N to 512. The sensitivity of the total number of particles to the results is discussed in Appendix A. Selection, resample, and mutation are processed according to the value of the potential functions, $G(x_{t,i})$, which designs the likelihood function in filtering problems (see section 2.5.4 about the potential function).

2.5.1. Genetic Selection Algorithm

The genetic selection algorithm selects those particles closer to the observations at the end of the assimilation window. We calculate the probability of the selections ("survival rate", $P_S(x_{t,i})$) for each particle and select particles according to their survival rate. In CLVDAS, the survival rates are defined as follows [*Rémy et al.*, 2012]:

$$P_s(x_{t,i}) = \frac{G(x_{t,i})}{\max_{x \in A} G(x_{t,j})}, \tag{19}$$

where A is the set that includes the state vectors of all particles before the selection and S is the set that includes the state vectors of only the selected particles.

2.5.2. Resampling Particles

Resampling is applied to generate new particles so as to replace rejected particles. We resample the particles by copying the surviving particles based on the weight of each particle:

$$w_{t,i} = \frac{G(x_{t,i})}{\sum_{x \in S} G(x_{t,j})}, \tag{20}$$

where $w_{t,i}$ represents the weights. Please note that we calculate weights only for the selected particles and $\sum_{x \in S} w_{t,i} = 1$. Having calculated the weights of the selected particles, they are resampled through an importance resampling algorithm using multinomial draws until we recover the original number of particles.

2.5.3. Mutation Process

To maintain the diversity of the particles, we add the fluctuation to the particles after the resampling process. For each vector component of a particle, the mutation process can be shown as follows:

$$x^k_{t,i,\mathrm{mutated}} = x^k_{t,i} + B^k \mu, \tag{21}$$

where $x^k_{t,i,\mathrm{mutated}}$ is the k-th vector component of particle i after the mutation process and μ is a random variable from a uniform distribution from -1 to 1. μ has a different number for the different vector components such that the magnitudes of perturbations are not correlated in the vertical. As *Kumar et al.* [2009] indicated, the correlation between soil moistures in vertical varies in the different regional climates and soil types. With no a priori information about this correlation, the assumption that the magnitudes of perturbations are not correlated in the vertical is reasonable. Please note that the strength of the surface and subsurface soil moisture coupling in the LSM has already affected the results of the data assimilation through the resampling process. The strength of the coupling is therefore not prescribed in this mutation process. B^k has a different value for each vector component of the particles. In this work, for surface soil moisture and LAI, we set both B^1 and B^{rn+1} to 0.0125. For root-zone soil moisture, we calculate this factor using the following equation:

$$B^k = B^1 \exp(-fz) \quad (k = 2, 3, \ldots, \mathrm{rn}), \tag{22}$$

where f is the decay factor, which is the same as the value of equation (6). The fluctuation of the mutation process decreases exponentially as the soil depth increases. This prevents unrealistic soil moisture profiles being generated by the LSM. We utilize the saturated hydraulic conductivity, which decreases exponentially with the decay factor, as a good proxy of the magnitude of soil moisture's change by the mutation process.

2.5.4. Design of the Potential Function

The potential function, $G(x_{t,i})$, should design the likelihood function. Here we construct this function as in the following:

$$G(x_{t,i}) = \exp(-\mathrm{COST_{GPF}}(x_{t,i})) \tag{23}$$

$$\mathrm{COST_{GPF}}(x_{t,i}) = \frac{1}{N_{\mathrm{obs}}} \sum_{t \in \mathrm{twindow}} \sum_{p=\mathrm{V,H}} \sum_{f=6.9\mathrm{GHz},10.7\mathrm{GHz},18.7\mathrm{GHz}} \frac{\left(T^{\mathrm{p,f}}_{\mathrm{b,est}} - T^{\mathrm{p,f}}_{\mathrm{b,obs}}\right)^2}{\left(\sigma + \left(T^{\mathrm{p,f}}_{\mathrm{b,est}} - T^{\mathrm{p,f}}_{\mathrm{b,obs}}\right)^2\right)}, \tag{24}$$

where N_{obs} is the total number of satellite scans in the assimilation window, twindow is the temporal length of the assimilation window, superscripts p and f indicate the polarization and frequency, respectively, and σ is a parameter that is set to 100 in this paper. We chose the Geman-McClure type estimator [*Geman and McClure*, 1987] for the potential function (see Figure S1 in the supporting information for the shape of this function). In this function with $\sigma = 100$, all biases which are over 30[K] nearly equally contribute to the potential function so that this estimator is relatively robust to outliers and suitable for stable implementation of GPF. Brightness temperatures at the same frequencies are used in Pass2 as in Pass1. In this paper, we set the duration of each assimilation window to 5 days. Although it could be set shorter, this assimilation window was selected to evaluate the vegetation growth rate of the particles. Because we can obtain several satellite observations in one assimilation window, we can evaluate every particle using multiple observations (the cost function is computed as the sum of the differences between all observed and the corresponding simulated brightness temperatures within the 5-day window), and the state vectors are adjusted every 5 days. Therefore, this implementation of the GPF works as a "smoother."

3. Data

3.1. In Situ Observation

We tested the CLVDAS at the Yanco Flux Tower site located in New South Wales, Australia. This site was used for validation of the soil moisture observed by AMSR2 onboard the Global Change Observation Mission-Water (GCOM-W) satellite. Observations of Yanco area were also used for retrieval of soil parameter of the LSM [*Bandara et al*., 2013, 2014], downscaling satellite-observed soil moisture data [*Piles et al*., 2011], and simulation of Soil Moisture Active Passive (SMAP) data stream [*Wu et al*., 2015]. We used the meteorological forcings (surface pressure, precipitation, surface air temperature, relative humidity, incoming shortwave radiation, incoming long-wave radiation, and wind speed) observed at this site to drive the CLVDAS.

In addition, we also used observations of ground soil moisture for validation of the CLVDAS. At this site, there are soil moisture probes at five depths (3, 10, 15, 45, and 75 cm); however, there were relatively low soil moisture contents at three depths (3, 10, and 45 cm) and very high soil moisture contents at two depths (15 and 75 cm) throughout almost the entire computational period. Without considering the strong vertical heterogeneity of soil characteristics, we cannot simulate these observed soil moistures. Therefore, only the data from the shallow depths (3 and 10 cm) were used for the validation process, while the results at the deeper depths are provided in the supporting information (Figure S2). In addition, the optimized parameter of equation (10) (see section 4 and Table 1) implies that more than 50% and 90% of root biomass is located in the top 10 and 30 cm soil depth, respectively (see also Figure S3). Although the top 100 cm is often considered the root zone, the deeper portion of this layer (i.e., 30–100 cm) does not strongly affect vegetation-soil moisture coupling in this instance. Because subsurface soil moisture is

Table 1. List of Important Parameters

Type	Symbol	Description	Value	Source
Hydrological	K_s	Saturated hydraulic conductivity	4.32×10^{-6}	Calibrated
	f	Vertical decay factor of saturated hydraulic conductivity	1.53	*Wang et al.* [2009c]
	θ_s	Saturation water content (porosity)	0.356	Calibrated
	α	Parameter in van Genuchten's water retention curve	0.0237	*FAO* [2003]
	n	Parameter in van Genuchten's water retention curve	1.61	Calibrated
Ecological	V_{max}	Maximum rubisco capacity of top leaf	8.63×10^{-5}	Calibrated
	d_{leaf}	Normal turnover rate of leaves [h^{-1}]	8.26×10^{-5}	Calibrated
	γ_{max}	Maximum water-related stress loss [h^{-1}]	0.00083	*Ivanov et al.* [2008]
	Ψ_{wilt}	The soil matric potentials at wilting point [Mpa]	−4.0	*Ivanov et al.* [2008]
	B	Empirical parameter of root biomass fraction function	0.926	Calibrated
Radiative transfer	l	Correlation length	1.79	Calibrated
	δ	RMS height	0.51	*Sawada and Koike* [2014b]
	b'	Vegetation parameter independent to wavelength	1.32	Sawada et al. (submitted)
	x	Vegetation parameter that shows the dependen ce of wavelength	−1.11	Sawada et al. (submitted)
	%sand[a]	Percentage of sand content	54.6	*Global Soil Data Task Group* [2000]
	%clay[a]	Percentage of clay content	22.7	*Global Soil Data Task Group* [2000]

[a]Note that soil texture parameters are used to calculate hydrological parameters through the pseudotransfer functions following *Yang et al.* [2009].

estimated by using data assimilation technology and vegetation-soil moisture coupling, only the depths where most of the root biomass is located are considered in the results.

3.2. Global Data Sets

We used the International Satellite Land Surface Climatology Project 2 soil data [*Global Soil Data Task Group*, 2000] to derive the soil texture. Initial guesses of the van Genuchten's water retention curve parameters [α and n; see equations (1)–(5)] were obtained from the Food and Agriculture Organization global data set [*Food and Agricultural Organization*, 2003].

The observed brightness temperatures were from the AMSR2 L3 product, whose native resolution is $0.1° \times 0.1°$. We used only night-scene data to reduce the effects of surface temperature bias on the optimization scheme. We also used retrieved soil water content from the AMSR2 L3 product [*Kachi et al.*, 2013] to compare the CLVDAS-estimated soil moisture with a soil moisture product from a single satellite. For the observed LAI, we used the MODIS MCD15A3 4-daily LAI product [*Huang et al.*, 2008] to evaluate the skill of the CLVDAS in simulating vegetation dynamics. Please note that satellite LAI products may have some biases and there are large differences between products [e.g., *Fang et al.*, 2013].

4. Experiment Design

We calculated the sensitivities of the parameters ($K_s, f, \theta_s, n, V_{max}, d_{leaf}, \gamma_{max}, \Psi_{wilt}, B$) to the brightness temperatures at every descending observation time of AMSR2. Please note that the "candidates" of optimized parameters listed above are slightly different from those in *Sawada and Koike* [2014b]. According to the values of the sensitivity indices (not shown), we found the parameters $f, \gamma_{max}, \Psi_{wilt}$ to be much less sensitive. Therefore, we calibrated $K_s, \theta_s, n, V_{max}, d_{leaf}, B$ as the unknown parameters of EcoHydro-SiB. We also included the correlation length in the RTM as a calibration parameter [*Sawada and Koike*, 2014b]. We implemented parameter optimization for these targeted parameters. Our calibrated parameters and other important parameters are listed in Table 1. In this paper, the results of the parameter optimization are not discussed in depth; please refer to *Sawada and Koike* [2014b] for additional details.

The GPF was run with the optimized parameters from 1 January 2013 to the end of 2013 (called the GPF simulation). We set the window to 5 days such that the particles were resampled every 5 days according to the values of their likelihood functions. In this paper, we used every particle that survived in the selection step of GPF (see section 2.5) to evaluate their probabilistic characteristics.

To evaluate the GPF capability, we additionally implemented a "pseudo-hindcast" experiment. In this numerical experiment, we first ran the CLVDAS with GPF during the specified duration, and then we ran every particle without any assimilation and adjustment [open loop (OL)]. We prepared four sets of this experiment according to the times of "release" of the particle: OL35day, OL100day, OL165day, and OL225day. For example, in the OL35day experiment, we ran the GPF simulation for the first 35 days followed by using the LSM (EcoHydro-SiB) without any data assimilation but using the initial conditions prepared by GPF for the rest of the computational period. Please note that any full forecasts were not implemented because the CLVDAS needs observed meteorological forcing data. In this "pseudo-hindcast" experiment, we extracted and evaluated the impact of initial conditions on land surface to the skill of simulating land surface conditions. We discuss the effect and importance of the initial conditions of root-zone soil moisture and LAI to forecasting ecohydrological conditions of the land surface in the following section.

Several metrics to evaluate our nonparametric data assimilation approach were used. First, Jensen-Shannon divergence (JSD) was used. JSD is calculated based on the Kullback-Leibler divergence (KLD) [*Cover and Thomas*, 1991; *Chou et al.*, 2011]:

$$D_{\mathrm{KL}}(p,q) = \sum_i p(i)\log\frac{p(i)}{q(i)} \tag{25}$$

where $D_{\mathrm{KL}}(p,q)$ is the KLD between two probabilistic distribution functions (PDFs), p and q. If two PDFs are equal for all i, $D_{\mathrm{KL}}(p,q)=0$. A small value for $D_{\mathrm{KL}}(p,q)$ indicates that p and q are close to each other, and therefore, the KLD is appropriate as a benchmark to evaluate the closeness of two PDFs [*Chou et al.*, 2011]. However, the KLD cannot be considered as a distance since this indicator is not symmetric ($D_{\mathrm{KL}}(p,q) \neq D_{\mathrm{KL}}(q,p)$). JSD can remedy this defect by formulating the following:

$$D_{\mathrm{JS}}(p,q) = \frac{1}{2}\left(D_{\mathrm{KL}}(p,r) + D_{\mathrm{KL}}(q,r)\right) \tag{26}$$

where $D_{\mathrm{JS}}(p,q)$ is JSD between PDF p and q, $r=\frac{1}{2}(p+q)$. If $p=q$, $D_{\mathrm{JS}}(p,q)=0$. In this study, JSD was calculated from the PDFs from simulated particles and observations. We assumed that the PDFs of observed soil moistures and LAI are normal distributions whose mean is the in situ and satellite-observed value. Standard deviation of observed soil moistures and LAI are chosen as 0.02 and 0.1, respectively (the choice of standard deviation does not considerably change our conclusions). In addition to the comparison of JSD, Pearson's correlation coefficient (R) was also calculated by comparing the median of the particles and observations. Bias and root mean square error (RMSE) were calculated both for median and for all particles:

$$\mathrm{bias}\,(\mathrm{median}) = \frac{1}{N_t}\sum_t\left(y_{\mathrm{median},t} - o_t\right) \tag{27}$$

$$\mathrm{bias}\,(\mathrm{allparticles}) = \frac{1}{N_t}\sum_t\left(\frac{1}{N_i}\sum_i\left(y_{i,t} - o_t\right)\right) \tag{28}$$

$$\mathrm{RMSE}\,(\mathrm{median}) = \frac{1}{N_t}\sum_t\sqrt{\left(y_{\mathrm{median},t} - o_t\right)^2} \tag{29}$$

$$\mathrm{RMSE}\,(\mathrm{allparticles}) = \frac{1}{N_t}\sum_t\left(\frac{1}{N_i}\sum_i\sqrt{\left(y_{i,t} - o_t\right)^2}\right) \tag{30}$$

where $y_{\mathrm{median},t}$ is the median value calculated from simulated particles at time t, $y_{i,t}$ is the simulated value from particle i at time t, o_t is the observed value at time t, N_t is the number of time steps, and N_i is the number of survived particles.

In addition to the experiments described above, the GPF simulation with prescribed LAI from MODIS was carried out. In this experiment, called noDVM, the DVM in EcoHydro-SiB was switched off, and our simulated LAI was replaced with MODIS LAI retrievals. In the CLVDAS, there are two pathways to improve our root-zone soil moisture estimation by using data assimilation: surface-subsurface soil moisture coupling and subsurface soil moisture-vegetation dynamics coupling. The purpose of noDVM simulation is to isolate the surface-subsurface soil moisture pathway. The results of the noDVM simulation can be found in Appendix B. The summary of the experimental design can be found in Table 2.

Table 2. Summary of Experiment Settings

Name	Description
GPF	Brightness temperatures are assimilated on the whole computational period
OL35day	Brightness temperatures are assimilated for the first 35 days
OL100day	Brightness temperatures are assimilated for the first 100 days
OL165day	Brightness temperatures are assimilated for the first 165 days
OL225day	Brightness temperatures are assimilated for the first 225 days
noDVM	Same as GPF but with prescribed LAI

5. Results and Discussion

First, we compare the GPF simulation with the OL35day simulation to demonstrate how the CLVDAS works and improves the skill of a land surface model. Figure 2 shows that the GPF brings no additional improvement to the simulation of surface soil moisture compared with the OL35day simulation. This is because the parameter-calibrated EcoHydro-SiB is already able to simulate surface soil moisture very accurately in the open loop scenario, without any adjustments. In addition, the climate memory of surface soil moisture in dry regions is short, such that adjustments of the initial conditions do not have a significant effect. Although we underestimate surface soil moisture in the wet season (June–September), we succeed in simulating it more accurately than the AMSR2 L3 soil water product which may not perfectly represent the point-scale soil moisture ground observations.

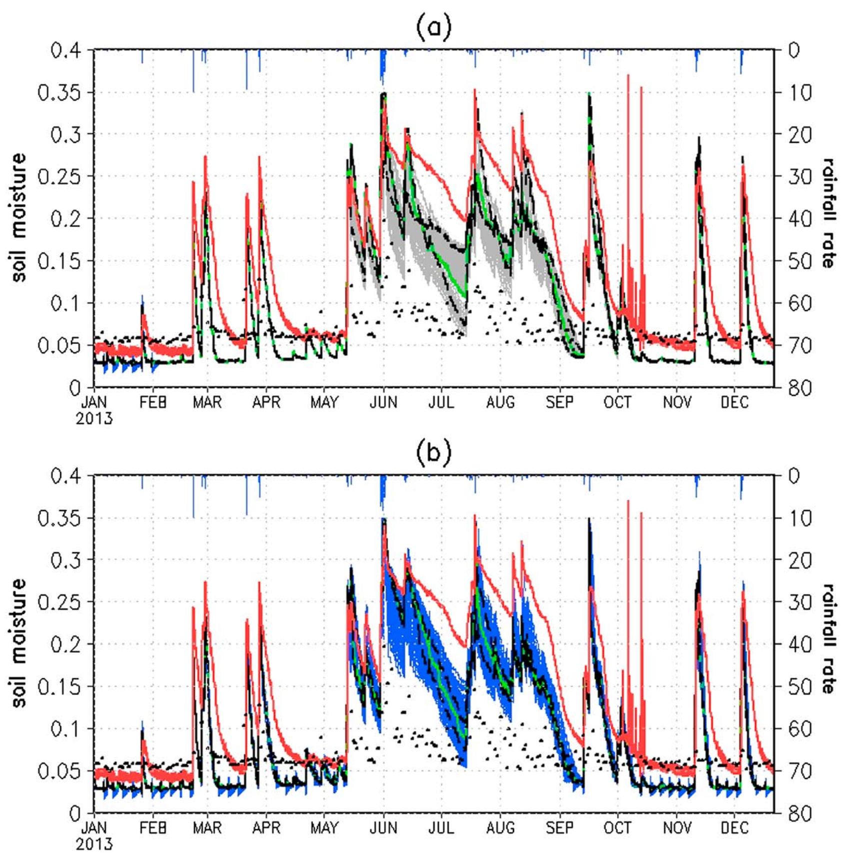

Figure 2. Time series of hourly near surface soil moisture [m^3/m^3] from (a) OL35day [genetic particle filtering (GPF) simulation was run for the first 35 days followed by using the EcoHydro-SiB without any data assimilation but using the initial conditions prepared by GPF for the rest of the computational period] and (b) genetic particle filtering (GPF) simulations. Each particle of the model-estimated 0 to 5 cm soil moistures from the open loop and GPF simulations is shown by the gray and blue lines, respectively. Green and black dashed lines are ensemble medians and quartiles, respectively. The red line is the in situ observed 3 cm soil moisture. Black dots are surface soil moisture observations from the AMSR2 L3 product. Hourly rainfall [mm/h] is also depicted as blue bars from the top.

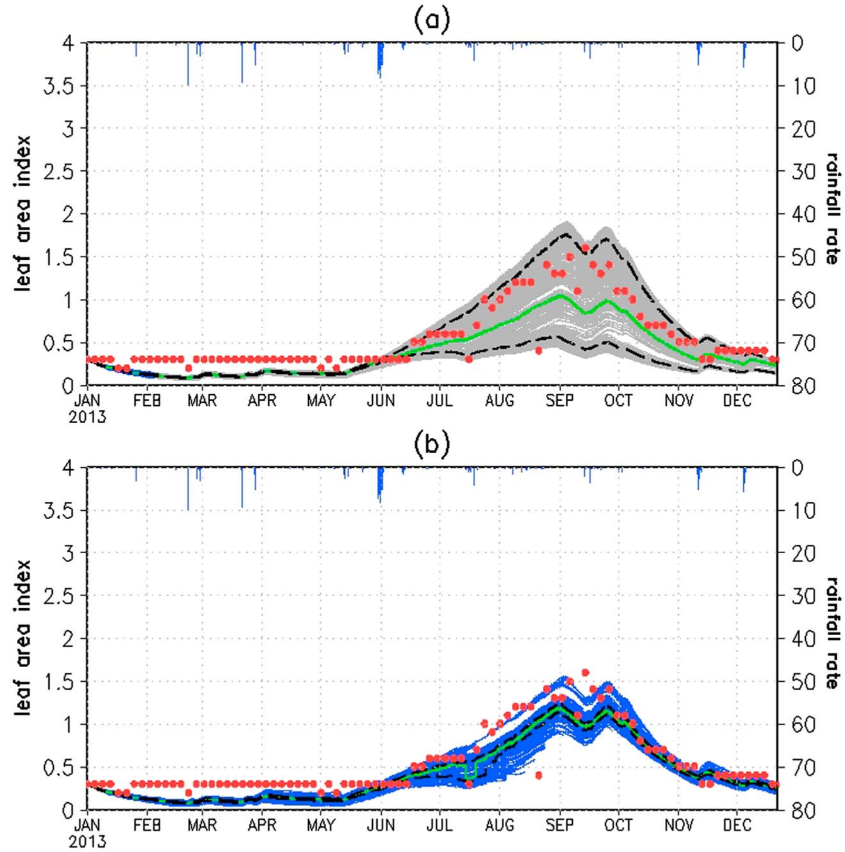

Figure 3. Time series of LAI [m^2/m^2] from (a) OL35day and (b) genetic particle filtering (GPF) simulations. Each particle of the model-estimated LAI from the open loop and GPF simulations is shown by the gray and blue lines, respectively. Green and black dashed lines are ensemble medians and quartiles, respectively. Red dots are MODIS satellite-observed LAI. Hourly rainfall [mm/h] is also depicted as blue bars from the top.

In contrast to soil moisture, we improve LAI estimation by using GPF. Figure 3 shows the LAI time series of the OL35day and GPF simulations. Although both simulations reproduce the seasonal cycle of vegetation growth and senescence, the OL35day simulation failed to estimate the absolute value of LAI. The GPF simulation succeeded in eliminating the particles that have small biomass amounts generated by the OL35day simulation and reproduced adequately the satellite-observed LAI phenology.

Figure 4 shows the distribution of LAI simulated by every particle at the end of the mature vegetation season (1 October). Figure 4a indicates that we cannot determine the biomass amount from the particles in the OL35day simulation, whereas the GPF simulation succeeds in conditioning particles for the estimation of LAI (Figure 4b).

Improvements in subsurface soil moisture estimation contribute to better estimations of LAI. Figures 5 and 6 show the time series of soil moisture at depths of 5–10 and 10–15 cm, respectively. Since dryer soil has lower hydraulic conductivity and wetter soil has higher hydraulic conductivity, the wetter particles respond more quickly to rainfall. The gray lines in Figures 5a and 6a show the bifurcation of root-zone soil moisture, especially from May to October. However, in the GPF simulation, the number of particles indicating low soil moisture content ($<10\%$) decreases rapidly at the beginning of August (Figures 5b and 6b). This is because these particles cannot reproduce the vegetation growth in this period, and thus, they are eliminated by the selection and resampling process of the GPF. The model-simulated root-zone soil moisture in the GPF simulation agrees well with in situ observations. Although we cannot observe directly the root-zone soil moisture from AMSR2, it can be inversely estimated from the vegetation signal of AMSR2 brightness temperatures through modeled soil moisture-vegetation dynamics coupling. However, please note that the CLVDAS can affect the skill of simulating soil moisture only in the layers where a large

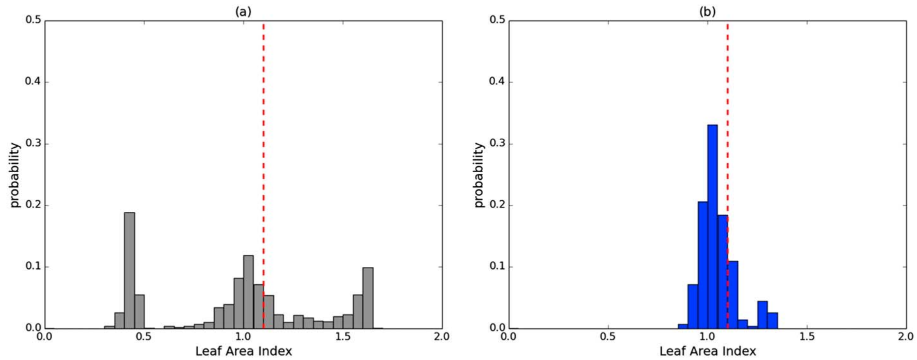

Figure 4. Histogram of particles of model-estimated LAI [m^2/m^2] from (a) OL35day and (b) genetic particle filtering (GPF) simulations at 00:00 (local time) on 1 October 2013. The red dashed line is the MODIS satellite-observed LAI at that time.

amount of root biomass is located as discussed in section 3.1 (see also Figure S2) since subsurface soil moisture-vegetation coupling is used for the improvement of subsurface soil moisture simulations. In Appendix B, we further discuss the impact of subsurface soil moisture-vegetation coupling to the estimation of root-zone soil moisture in GPF.

Figure 7 shows that the bifurcation between small soil moisture particles and large soil moisture particles lasts until the end of the mature vegetation period in the OL35day simulation, whereas it disappears in the GPF simulation. This causes the bifurcation of small LAI (≈0.5) particles and moderate LAI (≈1.0) particles in

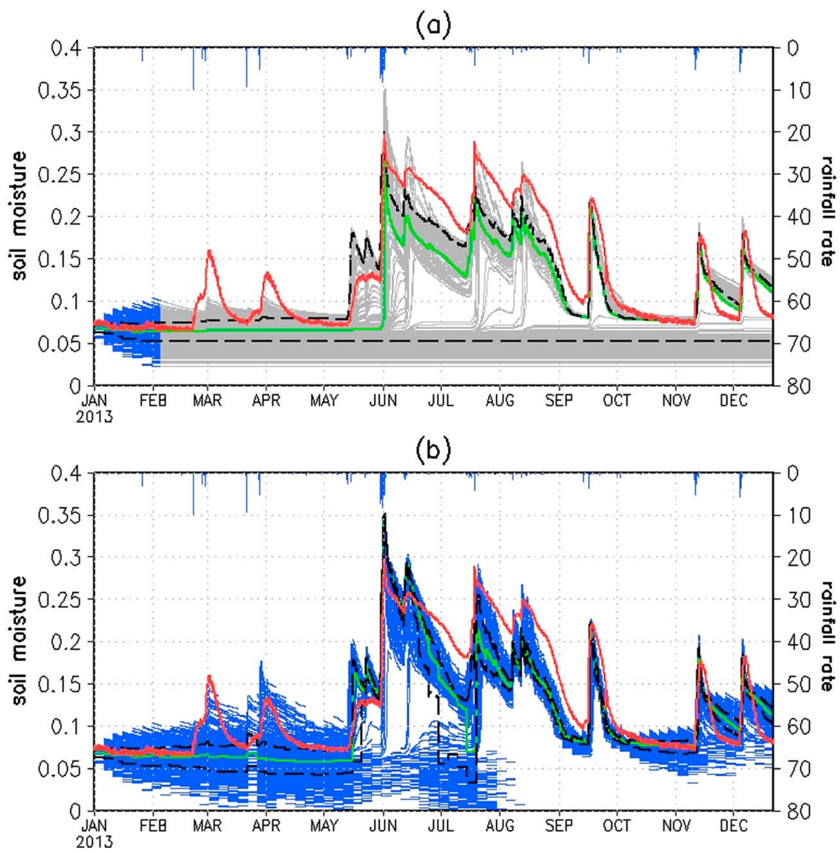

Figure 5. Time series of hourly 5 to 10 cm soil moisture [m^3/m^3] from (a) OL35day and (b) genetic particle filtering (GPF) simulations. Each particle of the model-estimated 5 to 10 cm soil moistures from the open loop and GPF simulations is shown by the gray and blue lines, respectively. Green and black dashed lines are ensemble medians and quartiles, respectively. The red line is the in situ observed 10 cm soil moisture. Hourly rainfall [mm/h] is also depicted as blue bars from the top.

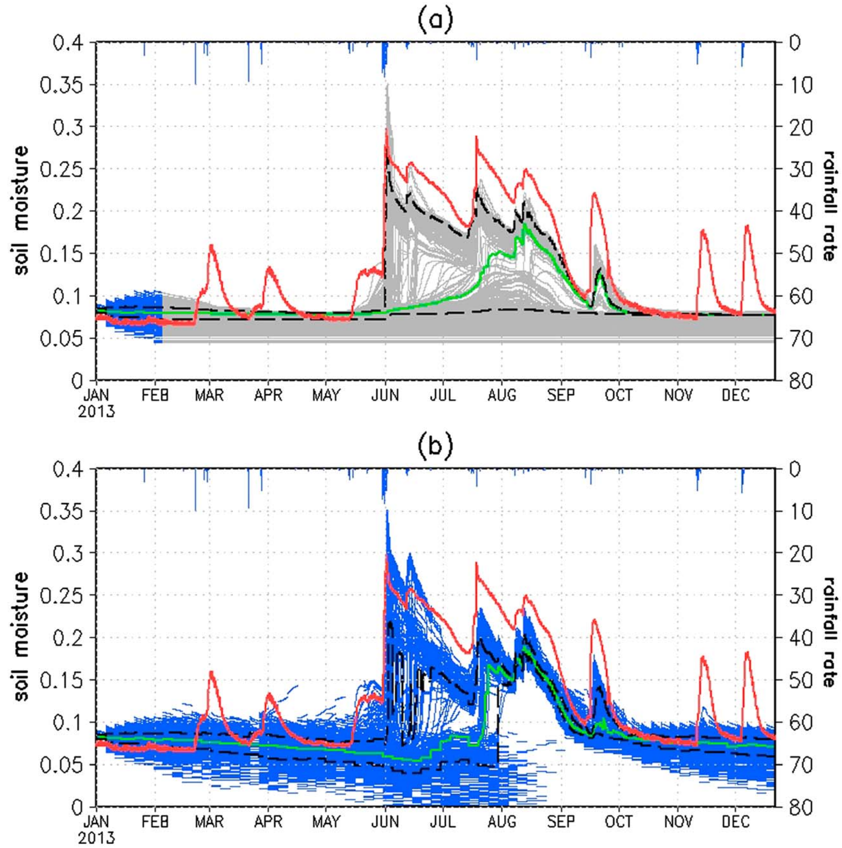

Figure 6. Time series of hourly 10 to 15 cm soil moisture [m^3/m^3] from (a) OL35day and (b) genetic particle filtering (GPF) simulations. Each particle of the model-estimated 10 to 15 cm soil moistures from the open loop and GPF simulations is shown by the gray and blue lines, respectively. Green and black dashed lines are ensemble medians and quartiles, respectively. The red line is the in situ observed 10 cm soil moisture. Hourly rainfall [mm/h] is also depicted as blue bars from the top.

Figure 4a. Larger LAI (≈1.6) particles are brought by other bifurcation in the deeper layer (not shown). We succeed to effectively condition particles and simulate root-zone soil moisture and LAI simultaneously in the GPF simulation (Figures 3b, 4b, 5b, 6b, and 7b).

Table 3 shows JSD, *R*, bias, and RMSE calculated from the data during the entire computational period (see also section 4 for the explanation of each metric). In JSD, GPF outperforms OL35day for LAI and soil moistures of three layers. However, the differences of JSD between GPF and OL35day are very small. This

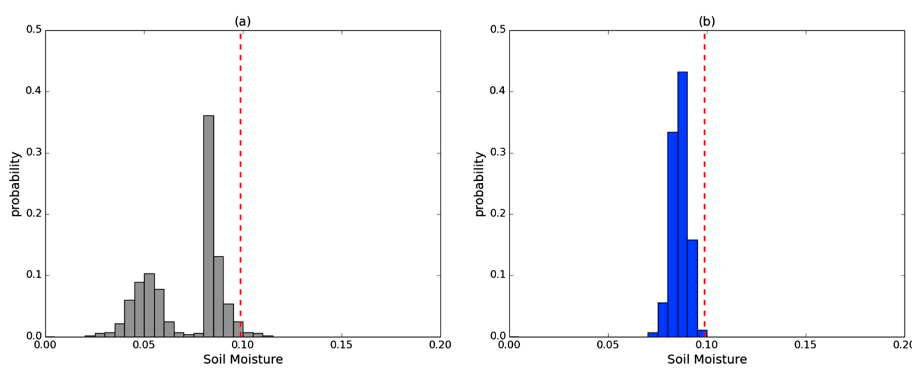

Figure 7. Histogram of particles of the model-estimated 5 to 10 cm soil moisture [m^3/m^3] from (a) OL35day and (b) genetic particle filtering (GPF) simulations at 00:00 (local time) on 1 October 2013. The red dashed line is the in situ observed 10-cm soil moisture at that time.

Table 3. CLVDAS Scores[a]

		GPF	OL35day	OL100day	OL165day	OL225day
LAI [m^2/m^2]	JSD	0.67	0.69	0.71	0.70	0.72
	R (median)	0.91	0.92	0.88	0.92	0.91
	Bias (median)	−0.13	−0.16	−0.26	−0.16	−0.14
	RMSE (median)	0.20	0.22	0.36	0.23	0.21
	Bias (all particles)	−0.13	−0.13	−0.2	−0.16	−0.15
	RMSE (all particles)	0.16	0.22	0.24	0.19	0.17
Soil moisture 0–5 cm [m^3/m^3]	JSD	1.43	1.48	1.42	1.41	1.46
	R (median)	0.93	0.93	0.92	0.95	0.93
	Bias (median)	−0.043	−0.041	−0.040	−0.038	−0.042
	RMSE (median)	0.055	0.054	0.053	0.047	0.054
	Bias (all particles)	−0.043	−0.041	−0.039	−0.039	−0.042
	RMSE (all particles)	0.045	0.043	0.042	0.041	0.045
Soil moisture 5–10 cm [m^3/m^3]	JSD	0.78	0.93	0.94	0.75	0.88
	R (median)	0.85	0.91	0.045	0.92	0.85
	Bias (median)	−0.021	−0.028	−0.056	−0.013	−0.020
	RMSE (median)	0.040	0.041	0.088	0.029	0.040
	Bias (all particles)	−0.026	−0.043	−0.050	−0.019	−0.025
	RMSE (all particles)	0.036	0.048	0.056	0.030	0.036
Soil moisture 10–15 cm [m^3/m^3]	JSD	0.94	1.00	1.00	1.04	1.02
	R (median)	0.42	0.66	0.25	−0.55	0.41
	Bias (median)	−0.047	−0.039	−0.055	−0.067	−0.046
	RMSE (median)	0.076	0.066	0.085	0.098	0.075
	Bias (all particles)	−0.045	−0.039	−0.051	−0.057	−0.046
	RMSE (all particles)	0.050	0.043	0.056	0.061	0.051

[a]JSD: Jensen-Shannon divergence; RMSE: root mean square error; *R*: Pearson's correlation coefficient. Simulated soil moistures in 5–10 and 10–15 cm are both evaluated by in situ observation at 10 cm depth.

is because observations are often located outside of the simulated PDF and this systematic error reduces the sensitivity of JSD. Table 3 also shows that although OL35day provides a large ensemble spread, the median of the particles can be a good estimator for both LAI and soil moistures (see also green and black dashed lines of Figures 3, 5, and 6). It indicates that the unknown parameters of our LSM have already been calibrated very well in Pass1. In 10–15 cm soil layer, soil moisture simulation is not improved by GPF in terms of *R*, bias, and RMSE due mainly to the large ensemble spread of GPF simulation in the outside of the growing seasons. Since the particles were released right after the beginning of simulation, the spread of particles in the beginning of the growing seasons is relatively small in OL35day. Because CLVDAS improves the skill of simulating subsurface soil moisture by using soil moisture-vegetation dynamics coupling, no improvements can be seen outside of the growing seasons. Therefore, we cannot find a significant improvement of the subsurface soil moisture simulation skill by GPF from the metrics, which is calculated for the entire computational period.

Figures 8–10 summarize the results of the other "pseudo-hindcasts," i.e., the OL100day, OL165day, and OL225day simulations. We evaluate how accurately each simulation reproduces soil moisture and LAI at

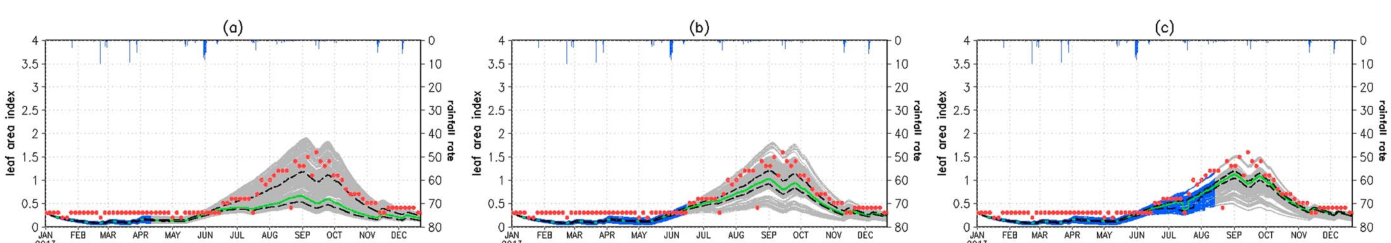

Figure 8. Time series of LAI [m^2/m^2] from (a) OL100day, (b) OL165day, and (c) OL225day simulations. Each particle of the model-estimated LAI from the open loop and genetic particle filtering (GPF) is shown by the gray and blue lines, respectively. Green and black dashed lines are ensemble medians and quartiles, respectively. The red dots are the MODIS satellite-observed LAI. Hourly rainfall [mm/h] is also depicted as blue bars from the top.

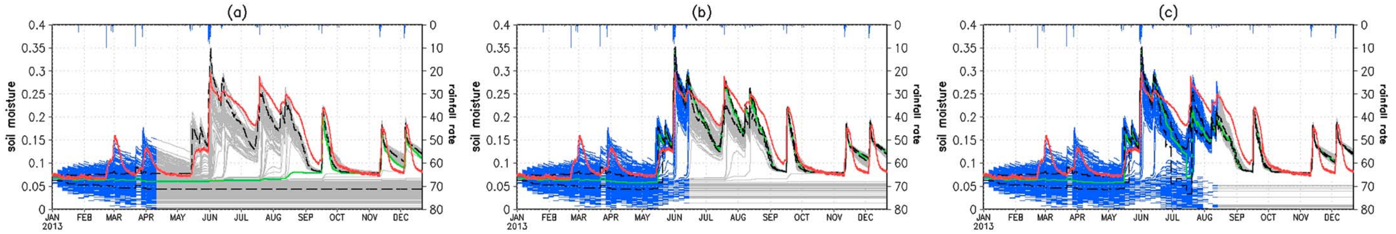

Figure 9. Time series of hourly 5 to 10 cm soil moisture [m^3/m^3]: (a) OL100day, (b) OL165day, and (c) OL225day simulations. Each particle of the model-estimated 5 to 10 cm soil moistures from the open loop and genetic particle filtering (GPF) is shown by the gray and blue lines, respectively. Green and black dashed lines are ensemble medians and quartiles, respectively. Red line is the in situ observed 10 cm soil moisture. Hourly rainfall [mm/h] is also depicted as blue bars from the top.

the end of mature vegetation period, based on information from only an LSM and the AMSR2 brightness temperatures, as performed above for the GPF and OL35day simulations. The OL100day, OL165day, and OL225day simulations were designed to provide approximately 6, 4, and 2 month lead times for forecasting the land surface condition on 1 October 2013, respectively. Because we used the same observed meteorological forcings for each offline simulation, the difference between the pseudo-hindcasts is caused only by the initial conditions of soil moisture and LAI.

Figure 8 shows that as the forecast lead time is reduced, the spread of LAI between each open loop particle (gray lines) gradually decreases. We cannot improve the skill if we stop assimilating outside of the vegetation growth season (OL100day; Figures 8a and 10a). Comparing the results of the OL35day simulation with those of OL100day, it was shown that data assimilation outside of the growing season brings no improvements to the estimation of land surface conditions in the growing seasons. Even though we shorten the forecasted lead time, no additional improvements can be expected by assimilating brightness temperatures outside of the growing seasons. However, when we release the particle in the growing seasons, an improvement is seen in the LAI estimation (OL165day and OL225day; Figures 8b, 8c, 10b, and 10c).

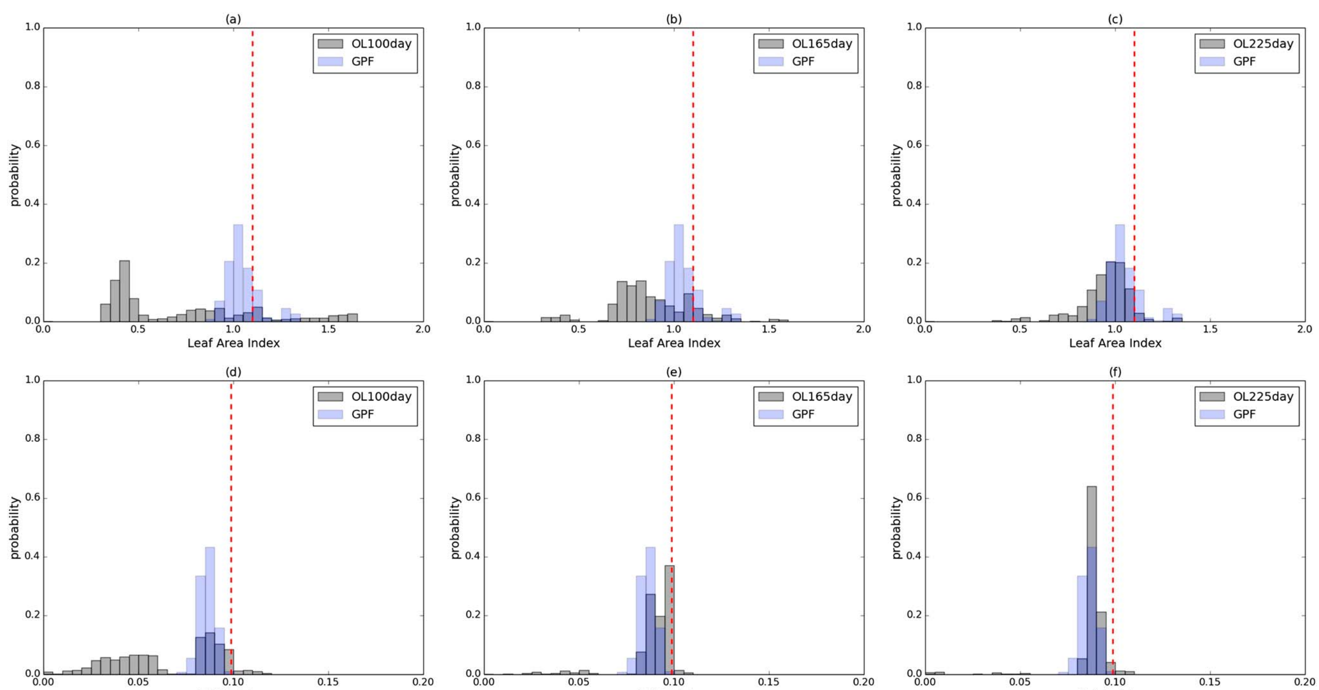

Figure 10. Histogram of particles of the model-estimated LAI [m^2/m^2] from (a) OL100day, (b) OL165day, and (c) OL225day simulations (gray bar) with genetic particle filtering (GPF) simulation (blue bar: same as Figure 4b) at 00:00 (local time) on 1 October 2013. The red dashed line is the MODIS satellite-observed LAI at that time. The histogram of particles of the model-estimated 5 to 10 cm soil moisture [m^3/m^3] from (d) OL100day, (e) OL165day, and (f) OL225day simulations (gray bar) with GPF simulation (blue bar: same as Figure 7b) at 00:00 (local time) on 1 October 2013. The red dashed line is the in situ observed 10 cm soil moisture at that time.

As discussed above, the improvement of the LAI simulation by GPF is strongly related to interactions between the root-zone soil moisture and vegetation dynamics. As we decrease the forecasted lead time, we can improve the estimation of root-zone soil moisture (Figure 9), which brings the significant improvement of LAI simulation skill. The shape of the histogram of the distribution of root-zone soil moisture of each particle at the end of the mature vegetation period gradually approaches that of the GPF simulation, as we decrease the forecasted lead time (Figures 10d–10f). Table 3 shows that in LAI and root-zone soil moisture, OL225day outperforms OL100day in terms of all metrics but JSD (the reason why JSD is less sensitive has been discussed above).

The initial conditions of subsurface soil moisture significantly affect the long-term simulation of biomass amount in water-controlled ecosystems, such that we should obtain the initial conditions of both root-zone soil moisture and LAI simultaneously. Because the initial condition of root-zone soil moisture can be successfully estimated by assimilating microwave observations, the CLVDAS can contribute to forecast LAI in up to 3 months.

6. Conclusions

In this study, we proposed a LDAS that can simulate surface soil moisture, subsurface soil moisture, and vegetation dynamics by assimilating passive microwave signals. Assimilating the AMSR2 brightness temperatures considerably improved the skill of an ecohydrological model in simulating both soil moisture and vegetation dynamics. To our knowledge, this is the first LDAS with a dynamic vegetation scheme that addresses the interactions of vegetation and subsurface soil moisture. Multi-frequency observations of AMSR series satellites, which are sensitive to both soil moisture and vegetation, make this development possible. In addition, the temporal fineness of low frequency microwave observations contributes to multi-target (i.e., soil moisture and vegetation dynamics) data assimilation, whose timescales are different.

As the initial conditions of subsurface soil moisture strongly affect skill in simulating vegetation dynamics, it is necessary to correctly and simultaneously obtain the initial conditions of soil moisture and vegetation dynamics. Although it is difficult to infer subsurface soil moisture from a data assimilation process for surface soil moisture in dry areas [e.g., *Kumar et al*., 2009], CLVDAS estimates root-zone soil moisture successfully in the growing season because of the modeled water-vegetation interaction process. The pseudo-hindcast experiments show that we can obtain an ensemble initial condition to correctly estimate soil moisture and LAI when the satellite observations are assimilated in the growing season, although data assimilation outside of the growing season brings no improvements to the estimation of land surface conditions in the growing seasons. The CLVDAS is a promising tool for the seasonal forecasting of ecohydrological conditions of the land surface.

Future work will focus on assimilating data from other satellite sensors [e.g., MODIS, GRACE, Soil Moisture and Ocean Salinity, and Soil Moisture Active Passive (SMAP)] and evaluating how these data contribute to improving further the skill of simulating the ecohydrological conditions of the land surface.

Appendix A: Sensitivity of the Number of Ensemble Members

To quantify the sensitivity of the number of ensemble members in our CLVDAS implementation, we calculated the PDFs of 5–10 cm soil moisture and LAI by using 32, 64, 128 and 256 ensemble members in addition to the implementation with 512 ensemble members. Then, the PDFs of each implementation are compared with that of the implementation with 512 ensemble members by calculating JSD (see also section 4).

Figure A1 shows the relationship between JSD and the number of ensemble members. Please note that in the case of 512 ensemble members, JSD = 0, because we compared the same PDFs. As the number of ensemble members is decreased, the shapes of PDF for both 5–10 cm soil moisture and LAI deviate from those of 512 ensemble members. However, this analysis indicates that our choice of 512 ensemble members is conservative. Considering the computational cost of continental or global application, the implementation with the smaller number of ensembles members (i.e., 128 or 256 ensembles) is feasible, although it should be noted that the sensitivity of the number of particles may not be same in the different regions and climates.

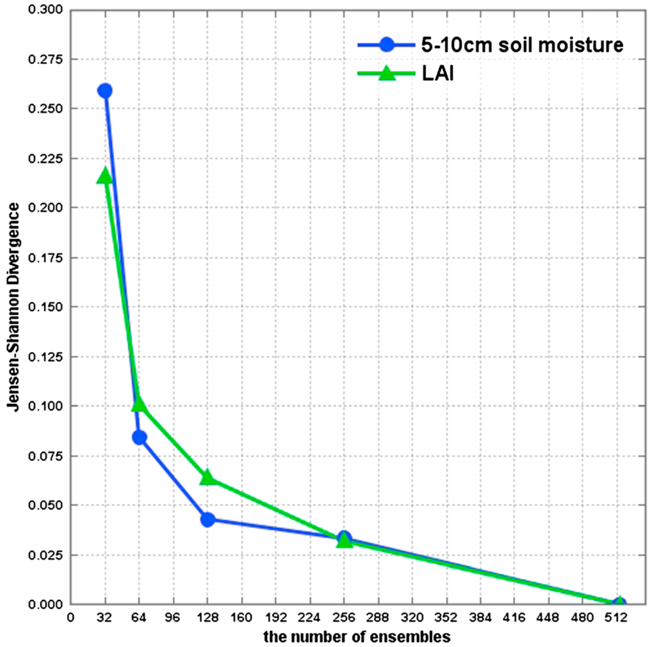

Figure A1. Relationship between Jensen-Shannon divergence (JSD) and the number of ensembles of GPF for 5–10 cm soil moisture (blue) and LAI (green). JSDs of GPF simulations with 32, 64, 128, 256, and 512 ensembles are calculated against GPF simulation with 512 ensembles.

Appendix B: Experiment Without DVM in CLVDAS

As discussed in section 4, the GPF simulation without DVM (noDVM simulation) was additionally carried out. In this numerical experiment, we used prescribed MODIS LAI directly and vegetation dynamics was not calculated inside of the CLVDAS. By analyzing the subsurface soil moisture in this experiment, the contribution of surface and subsurface soil moisture coupling to the skill of the CLVDAS in simulating root-zone soil moisture can be isolated.

Figure B1a shows that the bifurcation of 5–10 cm soil moisture can be resolved by using only surface-subsurface soil moisture coupling. The noDVM simulation can eliminate particles which indicate lower soil moisture as the GPF simulation can, although the original GPF simulation

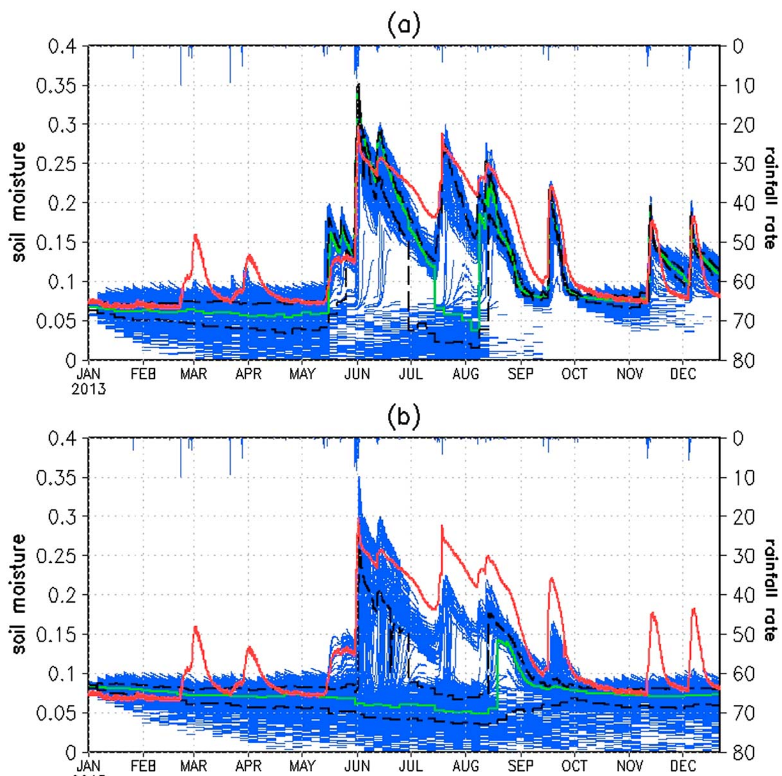

Figure B1. (a) Time series of hourly 5 to 10 cm soil moisture [m^3/m^3] and (b) time series of hourly 10–15 cm soil moisture in noDVM simulation. Each particle of the model-estimated soil moistures is shown by blue lines. Green and black dashed lines are ensemble medians and quartiles, respectively. The red line is the in situ observed 10 cm soil moisture. Hourly rainfall [mm/h] is also depicted as blue bars from the top.

eliminates these particles much faster than noDVM simulation does (please compare Figure 5b with Figure B1a).

However, the effect of surface and subsurface soil moisture coupling decreases as the depth increases. Figure B1b shows we cannot completely eliminate lower soil moisture particles of a 10–15 cm soil layer in noDVM simulation. By comparing Figure 6b with Figure B1b, we can see that subsurface soil moisture-vegetation dynamics coupling significantly affects the soil moisture estimation of this layer in the CLVDAS.

The noDVM simulation clearly shows that the CLVDAS has two different pathways to improve root-zone soil moisture: surface-subsurface soil moisture coupling and subsurface soil moisture-vegetation dynamics coupling. The CLVDAS effectively and simultaneously use these two pathways in order to simulate soil moisture and vegetation dynamics.

Acknowledgments
Surface observation data from the Yanco site were furnished by the Japan Aerospace Exploration Agency (JAXA), in collaboration with Monash University (the data can be available upon request to the authors). The AMSR2 brightness temperature observations and surface soil moisture product were provided by the JAXA and can be downloaded at https://gcom-w1.jaxa.jp/auth.html. MCD15A3 LAI products were provided by the National Aeronautics and Space Administration (NASA) and can be downloaded at https://earthdata.nasa.gov/. The authors acknowledge Frank Winston and Sandra Monerris-Belda for their field work. The authors are supported by the Data Integration & Analysis System in providing the data and the data integration resources. Yohei Sawada is supported by the Japan Society for the Promotion of Science. The authors thank four anonymous reviewers for their helpful advice.

References

Albergel, C., J.-C. Calvet, J.-F. Mahfouf, C. Rüdiger, A. L. Barbu, S. Lafont, J.-L. Roujean, J. P. Walker, M. Crapeau, and J.-P. Wigneron (2010), Monitoring of water and carbon fluxes using a land data assimilation system: A case study for southwestern France, *Hydrol. Earth Syst. Sci.*, *14*, 1109–1124, doi:10.5194/hess-14-1109-2010.

Albergel, C., P. de Rosnay, C. Gruhier, J. Munos-Sabater, S. Hasenauer, L. Isaksen, Y. Kerr, and W. Wagner (2012), Evaluation of remotely sensed and modelled soil moisture products using global ground-based in situ observation, *Remote Sens. Environ.*, *118*, 215–226, doi:10.1016/j.rse.2011.11.017.

Arora, V. K., and G. J. Boer (2005), A parameterization of leaf phenology for the terrestrial ecosystem component of climate models, *Global Change Biol.*, *11*, 39–59, doi:10.1111/j.1365-2486.2004.00890.x.

Bandara, R., J. P. Walker, and C. Rüdiger (2013), Towards soil property retrieval from space: A one-dimensional twin-experiment, *J. Hydrol.*, *497*, 198–207, doi:10.1016/j.jhydrol.2013.06.004.

Bandara, R., J. P. Walker, and C. Rüdiger (2014), Towards soil property retrieval from space: Proof of concept using in situ observations, *J. Hydrol.*, *512*, 27–38, doi:10.1016/j.jhydrol.2014.02.031.

Bardu, A. L., J.-C. Calvet, J.-F. Mahfouf, C. Albergel, and S. Lafont (2011), Assimilation of Soil Wetness Index and Leaf Area Index into the ISBA-A-gs land surface model: Grassland case study, *Biogeosciences*, *8*, 1971–1986, doi:10.5194/bg-8-1971-2011.

Beven, K. (1982), On subsurface stormflow: An analysis of response times, *Hydrol. Sci. J.*, *27*, 505–521, doi:10.1080/02626668209491129.

Boussetta, S., et al. (2013), Natural land carbon dioxide exchanges in the ECMWF integrated forecasting system: Implementation and offline validation, *J. Geophys. Res. Atmos.*, *118*, 5923–5946, doi:10.1002/jgrd.50488.

Cabral, M. L. G., R. Bras, and D. Entekhabi (1992), A kinematic model of infiltration and runoff generation in layered and sloped soils, *Adv. Water Resour.*, *15*, 311–324, doi:10.1016/0309-1708(92)90017-V.

Calvet, J., J. Noilhan, J. Roujean, P. Bessemoulin, M. Cabelguenne, A. Olioso, and J. Wigneron (1998), An interactive vegetation SVAT model tested against data from six contrasting sites, *Agric. For. Meteorol.*, *92*, 73–95.

Chou, R., Y. Boers, M. Podt, and M. Geist (2011), Performance evaluation for particle filters, in *Proceedings of the 14th International Conference on Information Fusion (FUSION)*, pp. 1–7, IEEE, Piscataway, N. J.

Ciocca, F., I. Lunati, and M. B. Parlange (2014), Effects of the water retention curve on evaporation from arid soils, *Geophys. Res. Lett.*, *41*, 3110–3116, doi:10.1002/2014GL059827.

Clark, D., et al. (2011), The Joint UK Land Environmental Simulator (JULES), model description—Part 2: Carbon fluxes and vegetation dynamics, *Geosci. Model Dev.*, *4*, 701–722, doi:10.5194/gmd-4-701-2011.

Cover, T. M., and J. A. Thomas (1991), *Elements of Information Theory*, Wiley, Hoboken, N. J.

Duan, Q., S. Sorooshian, and V. Gupta (1992), Effective and efficient global optimization for conceptual rainfall-runoff models, *Water Resour. Res.*, *28*, 1015–1031, doi:10.1029/91WR02985.

Fang, H., et al. (2013), Characterization and intercomparison of global moderate resolution leaf area index (LAI) products: Analysis of climatologies and theoretical uncertainties, *J. Geophys. Res. Biogeosci.*, *118*, 529–548, doi:10.1002/jgrg.20051.

Food and Agricultural Organization (2003), Digital soil map of the world and derived soil properties, Land Water Digital Media Ser. 1 [CR- ROM], Rome. [Available at http://www.fao.org/ag/agl/lwdms.stm.]

Garcia-Carreras, L., and D. J. Parker (2011), How does local tropical deforestation affect rainfall?, *Geophys. Res. Lett.*, *38*, L19802, doi:10.1029/2011GL049099.

Geman, S., and D. E. McClure (1987), Statistical methods for tomographic image reconstruction, *Bull. Int. Statist. Inst.*, *LII*(4), 5–21.

Global Soil Data Task Group (2000), Global gridded surfaces of selected soil characteristics (IGBPDIS). [Available at http://www.daac.ornl.gov/.]

Gruhier, C., P. de Rosnay, Y. Kerr, E. Mougin, E. Ceschia, J. C. Calvet, and P. Richaume (2008), Evaluation of AMSR-E soil moisture product based on ground measurements over temperate and semi-arid regions, *Geophys. Res. Lett.*, *35*, L10405, doi:10.1029/2008GL033330.

Hohenegger, C., P. Brockhaus, C. S. Bretherton, and C. Schär (2009), The soil moisture-precipitation feedback in simulations with explicit and parameterized convection, *J. Clim.*, *22*, 5003–5020, doi:10.1175/2009JCLI2604.1.

Huang, D., Y. Knyazikhin, W. Wang, D. W. Deering, P. Stenberg, N. Shabanov, B. Tan, and R. B. Myneni (2008), Stochastic transport theory for investigating the three-dimensional canopy structure from space measurements, *Remote Sens. Environ.*, *112*(1), 35–50.

Ivanov, V. Y., R. L. Bras, and E. R. Vivoni (2008), Vegetation-hydrology dynamics in complex terrain of semiarid areas: 1. A mechanistic approach to modeling dynamic feedbacks, *Water Resour. Res.*, *44*, W03429, doi:10.1029/2006WR005588.

Jackson, R. B., J. Canadell, J. R. Ehleringer, H. A. Mooney, Q. E. Sala, and E. D. Schulze (1996), A global analysis of root distributions for terrestrial biomes, *Oecologia*, *108*, 389–411.

Jackson, T. J., and T. J. Schmugge (1991), Vegetation effects on the microwave emission of soils, *Remote Sens. Environ.*, *36*, 203–202, doi:10.1016/0034-4257(91)90057-D.

Jackson, T. J., M. H. Cosh, R. Bindlish, P. J. Starks, D. D. Bosch, M. Seyfried, D. C. Goodrich, M. S. Moran, and J. Du (2010), Validation of advanced microwave scanning radiometer soil moisture products, *IEEE Trans. Geosci. Remote.*, *48*, 4256–4272.

Jaranilla-Sanchez, P. A., L. Wang, and T. Koike (2011), Modeling the hydrological responses of the Pampanga River basin, Philippines: A quantitative approach for identifying droughts, *Water Resour. Res.*, *47*, W03514, doi:10.1029/2010WR009702.

Jarlan, L., G. Balsamo, S. Lafont, A. Beljaars, J. C. Calvet, and E. Mougin (2008), Analysis of leaf area index in the ECMWF land surface model and impact on latent heat and carbon fluxes: Application to West Africa, *J. Geophys. Res.*, *113*, D24117, doi:10.1029/2007JD009370.

Jones, M. O., L. A. Jones, J. S. Kimball, and K. C. McDonald (2011), Satellite passive microwave remote sensing for monitoring global land surface phenology, *Remote Sens. Environ.*, *115*, 1102–1114, doi:10.1016/j.rse.2010.12.015.

Kachi, M., K. Naoki, M. Hori, and K. Imaoka (2013), AMSR2 validation results, in *IEEE International Geoscience and Remote Sensing Symposium (IGARSS)*, pp. 831–834, IEEE, Piscataway, N. J., doi:10.1109/IGARSS.2013.6721287.

Kumar, S. V., R. H. Reichle, R. D. Koster, W. T. Crow, and C. D. Peters-Lidard (2009), Role of subsurface physics in the assimilation of surface soil moisture observations, *J. Hydrometeorol.*, *10*, 1534–1547, doi:10.1175/2009JHM1134.1.

Kuria, D. N., T. Koike, H. Lu, H. Tsutsui, and T. Graf (2007), Field-supported verification and improvement of a passive microwave surface emission model for rough, bare, and wet soil surfaces by incorporating shadowing effects, *IEEE Trans. Geosci. Remote.*, *45*, 1207–1216.

Kwok, N., and W. Zhou (2005), Evolutionary particle filter: Re-sampling from the genetic algorithm perspective, in *2005 IEEE/RSJ International Conference on Intelligent Robots and Systems*, pp. 2935–2940, IEEE, Piscataway, N. J., doi:10.1109/IROS.2005.1545119.

Lawrence, D. M., et al. (2011), Parameterization improvements and functional and structural advances in version 4 of the community land model, *J. Adv. Model. Earth Syst.*, *3*, M03001, doi:10.1029/2011MS00045.

Li, B., D. Toll, X. Zhan, and B. Cosgrove (2012a), Improving estimated soil moisture fields through assimilation of AMSR-E soil moisture retrievals with an ensemble Kalman filter and a mass conservation constraint, *Hydrol. Earth Syst. Sci.*, *16*, 105–119, doi:10.5194/hess-16-105-2012.

Li, B., M. Rodell, B. F. Zaitchik, R. H. Reichle, R. D. Koster, and T. M. van Dam (2012b), Assimilation of GRACE terrestrial water storage into a land surface model: Evaluation and potential value for drought monitoring in western and central Europe, *J. Hydrol.*, *446–447*, 103–115, doi:10.1016/j.jhydrol.2012.04.035.

Liu, Y. Y., R. A. M. de Jeu, M. F. McCabe, J. P. Evans, and A. I. J. M. van Dijk (2011), Global long-term passive microwave satellite-based retrieval of vegetation optical depth, *Geophys. Res. Lett.*, *38*, L18402, doi:10.1029/2011GL048684.

Marzban, C. (2013), Variance-based sensitivity analysis: An illustration on the Lorenz'63 model, *Mon. Weather Rev.*, *141*, 4069–4079, doi:10.1175/MWR-D-13-00032.1.

Mechri, R., C. Ottlé, O. Pannekoucke, and A. Kallel (2014), Genetic particle filter application to land surface temperature downscaling, *J. Geophys. Res. Atmos.*, *119*, 2131–2146, doi:10.1002/2013JD020354.

Mo, T., B. J. Choudhury, T. J. Schmugge, J. R. Wang, and T. J. Jackson (1982), A model for microwave emission from vegetation-covered fields, *J. Geophys. Res.*, *87*, 11,229–11,237, doi:10.1029/JC087iC13p11229.

Montzka, C., V. R. N. Pauwels, H.-J. H. Franssen, X. Han, and H. Vereecken (2012), Multivariate and multiscale data assimilation in terrestrial systems: A review, *Sensors*, *12*, 16,291–16,333, doi:10.3390/s121216291.

Nearing, G. S., W. T. Crow, K. R. Thorp, M. S. Moran, R. H. Reichle, and H. V. Gupta (2012), Assimilating remote sensing observations of leaf area index and soil moisture for wheat yield estimates: An observing system simulation experiment, *Water Resour. Res.*, *48*, 1–13, doi:10.1029/2011WR011420.

Njoku, E. G., T. J. Jackson, V. Lakshmi, T. K. Chan, and S. V. Nghiem (2003), Soil moisture retrieval from AMSR-E, *IEEE Trans. Geosci. Remote.*, *41*, 215–229.

Owe, M., R. de Jeu, and J. Walker (2001), A methodology for surface soil moisture and vegetation optical depth retrieval using the microwave polarization difference index, *IEEE Trans. Geosci. Remote.*, *39*, 1643–1654, doi:10.1109/36.942542.

Owe, M., R. de Jeu, and T. Holmes (2008), Multisensor historical climatology of satellite-derived global land surface moisture, *J. Geophys. Res.*, *113*, F01002, doi:10.1029/2007JF000769.

Paloscia, S., and P. Pampaloni (1988), Microwave polarization index for monitoring vegetation growth, *IEEE Trans. Geosci. Remote.*, *26*, 617–621, doi:10.1109/36.7687.

Paloscia, S., G. Macelloni, E. Santi, and T. Koike (2001), A multifrequency algorithm for the retrieval of soil moisture on a large scale using microwave data from SMMR and SSM/I satellites, *IEEE Trans. Geosci. Remote.*, *39*, 1655–1661, doi:10.1109/36.942543.

Pan, M., X. Yuan, and E. F. Wood (2013), A probabilistic framework for assessing drought recovery, *Geophys. Res. Lett.*, *40*, 3637–3642, doi:10.1002/grl.50728.

Pappas, C., S. Fatichi, S. Leuzinger, A. Wolf, and P. Burlando (2013), Sensitivity analysis of a process-based ecosystem model: Pinpointing parameterization and structural issues, *J. Geophys. Res. Biogeosci.*, *118*, 505–528, doi:10.1002/jgrg.20035.

Piles, M., A. Camps, M. Vall-llossera, I. Corbella, R. Panciera, C. Rudiger, Y. H. Kerr, and J. Walker (2011), Downscaling SMOS-derived soil moisture using MODIS visible/infrared data, *IEEE Trans. Geosci. Remote.*, *49*, 3156–3166, doi:10.1109/TGRS.2011.2120615.

Qin, J., S. Liang, K. Yang, I. Kaihotsu, R. Liu, and T. Koike (2009), Simultaneous estimation of both soil moisture and model parameters using particle filtering method through the assimilation of microwave signal, *J. Geophys. Res.*, *114*, D15103, doi:10.1029/2008JD011358.

Rasmy, M., T. Koike, S. Boussetta, H. Lu, and X. Li (2011), Development of a satellite land data assimilation system coupled with a mesoscale model in the Tibetan Plateau, *IEEE Trans. Geosci. Remote.*, *49*, 2847–2862.

Rémy, S., O. Pannekoucke, T. Bergot, and C. Baehr (2012), Adaptation of a particle filtering method for data assimilation in a 1D numerical model used for fog forecasting, *Q. J. R. Meteorol. Soc.*, *138*, 536–551.

Robinson, J., and M. Sivapalan (1996), Instantaneous response functions of overland flow and subsurface stormflow for catchment models, *Hydrol. Processes*, *10*, 845–862, doi:10.1002/(SICI)1099-1085(199606)10:6<845::AID-HYP375>3.0.CO;2-7.

Saavedra, O., T. Koike, K. Yang, T. Graf, X. Li, L. Wang, and X. Han (2010), Decision support for dam release during floods using a distributed biosphere hydrological model driven by quantitative precipitation forecasts, *Water Resour. Res.*, *46*, W10544, doi:10.1029/2010WR009502.

Sabater, J. M., C. Rüdiger, J.-C. Calvet, N. Fritz, L. Jarlan, and Y. Kerr (2008), Joint assimilation of surface soil moisture and LAI observations into a land surface model, *Agric. For. Meteorol.*, *148*, 1362–1373, doi:10.1016/j.agriformet.2008.04.003.

Saltelli, A., P. Annoni, I. Azzini, F. Campolongo, M. Ratto, and S. Tarantola (2010), Variance based sensitivity analysis of model output. Design and estimator for the total sensitivity index, *Comput. Phys. Commun.*, *181*(2), 259–270, doi:10.1016/j.cpc.2009.09.018.

Samain, O., L. Kergoat, P. Hiernaux, F. Guichard, E. Mougin, F. Timouk, and F. Laveau (2008), Analysis of the in situ and MODIS albedo variability at multiple timescales in the Sahel, *J. Geophys. Res.*, *113*, D14119, doi:10.1029/2007JD009174.

Sanchez-Mejia, Z. M., and S. A. Papuga (2014), Observations of a two-layer soil moisture influence on surface energy dynamics and planetary boundary layer characteristics in a semiarid shrubland, *Water Resour. Res.*, *50*, 306–317, doi:10.1002/2013WR014135.

Sanchez-Mejia, Z. M., S. A. Papuga, J. B. Swetish, W. van Leeuwen, D. Szutu, and K. Hartfield (2014), Quantifying the influence of deep soil moisture on ecosystem albedo: The role of vegetation, *Water Resour. Res.*, *50*, 4038–4053, doi:10.1002/2013WR014150.

Sawada, Y., and T. Koike (2013), Development of a distributed hydrological-dynamic vegetation coupling model and its application to North Africa [in Japanese], *J. Jpn. Soc. Civil Eng. Ser. B1 (Hydraulic Engineering)*, *69*(4).

Sawada, Y., and T. Koike (2014a), Development of the optimization scheme of the hydrological-ecological coupling model assimilating microwave signal [in Japanese], *J. Jpn. Soc. Civil Eng. Ser. B1 (Hydraulic Engineering)*, *70*(4).

Sawada, Y., and T. Koike (2014b), Simultaneous estimation of both hydrological and ecological parameters in an ecohydrological model by assimilating microwave signal, *J. Geophys. Res. Atmos.*, *119*, 8839–8857, doi:10.1002/2014JD021536.

Sawada, Y., T. Koike, and P. A. Jaranilla-Sanchez (2014), Modeling hydrologic and ecologic responses using a new eco-hydrological model for identification of droughts, *Water Resour. Res.*, *50*, 6214–6235, doi:10.1002/2013WR014847.

Sellers, P. J., D. A. Randall, G. J. Collatz, J. A. Berry, C. B. Field, D. A. Dazlich, C. Zhang, G. D. Collelo, and L. Bounoua (1996), A revised land surface parameterization (SiB2) for atmospheric GCMs, Part I: Model formulation, *J. Clim.*, *9*, 676–705.

Stöckli, R., T. Rutishauser, D. Dragoni, J. O'Keefe, P. E. Thornton, M. Jolly, L. Lu, and A. S. Denning (2008), Remote sensing data assimilation for a prognostic phenology model, *J. Geophys. Res.*, *113*, G04021, doi:10.1029/2008JG000781.

Stöckli, R., T. Rutishauser, I. Baker, M. A. Liniger, and A. S. Denning (2011), A global reanalysis of vegetation phenology, *J. Geophys. Res.*, *116*, G03020, doi:10.1029/2010JG001545.

Su, Z., P. de Rosnay, J. Wen, L. Wang, and Y. Zeng (2013), Evaluation of ECMWF's soil moisture analyses using observations on the Tibetan Plateau, *J. Geophys. Res. Atmos.*, *118*, 5304–5318, doi:10.1002/jgrd.50468.

Tian, X., Z. Xie, A. Dai, C. Shi, B. Jia, F. Chen, and K. Yang (2009), A dual-pass variational data assimilation framework for estimating soil moisture profiles from AMSR-E microwave brightness temperature, *J. Geophys. Res.*, *114*, D16102, doi:10.1029/2008JD011600.

Timouk, F., L. Kergoat, E. Mougin, C. R. Lloyd, E. Ceschia, J. M. Cohard, P. de Rosnay, P. Hiernaux, V. Demarez, and C. M. Taylor (2009), Response of surface energy balance to water regime and vegetation development in a Sahelian landscape, *J. Hydrol.*, *375*, 178–189.

Uosaki, K., Y. Kimura, and T. Hatanaka (2004), Evolution strategies based particle filters for state and parameter estimation on nonlinear models, in *Proceedings of the 2004 Congress on Evolutionary Computation (IEEE Cat. No. 04TH8753)*, pp. 884–890, IEEE, doi:10.1109/CEC.2004.1330954.

Van Genuchten, M. T. (1980), A closed-form equation for predicting the hydraulic conductivity of unsaturated soils, *Soil Sci. Soc. Am. J.*, *44*, 892–898.

Vrugt, J. A., C. J. F. ter Braak, C. G. H. Diks, and G. Schoups (2013), Hydrologic data assimilation using particle Markov chain Monte Carlo simulation: Theory, concepts and applications, *Adv. Water Resour.*, *51*, 457–478, doi:10.1016/j.advwatres.2012.04.002.

Wang, F., L. Wang, T. Koike, H. Zhou, K. Yang, A. Wang, and W. Li (2011), Evaluation and application of a fine-resolution global data set in a semiarid mesoscale river basin with a distributed biosphere hydrological model, *J. Geophys. Res.*, *116*, D21108, doi:10.1029/2011JD015990.

Wang, L., T. Koike, K. Yang, T. Jackson, R. Bindlish, and D. Yang (2009a), Development of a distributed biosphere hydrological model and its evaluation with the Southern Great Plains Experiments (SGP97 and SGP99), *J. Geophys. Res.*, *114*, D08107, doi:10.1029/2008JD010800.

Wang, L., T. Koike, K. Yang, and P. Yeh (2009b), Assessment of a distributed biosphere hydrological model against streamflow and MODIS land surface temperature in the upper Tone River Basin, *J. Hydrol.*, *377*, 21–34.

Wang, L., T. Koike, D. Yang, and K. Yang (2009c), Improving the hydrology of the Simple Biosphere Model 2 and its evaluation within the framework of a distributed hydrological model, *Hydrol. Sci. J.*, *54*(6), 989–1006.

Wood, A. W., and D. P. Lettenmaier (2008), An ensemble approach for attribution of hydrologic prediction uncertainty, *Geophys. Res. Lett.*, *35*, L14401, doi:10.1029/2008GL034648.

Wu, X., J. P. Walker, and C. Rüdiger (2015), Simulation of the SMAP data stream from SMAPEx field campaigns in Australia, *IEEE Trans. Geosci. Remote.*, *53*, 1921–1934, doi:10.1109/TGRS.2014.2350988.

Xue, B.–L., et al. (2013), Modeling the land surface water and energy cycles of a mesoscale watershed in the central Tibetan Plateau during summer with a distributed hydrological model, *J. Geophys. Res. Atmos.*, *118*, 8857–8868, doi:10.1002/jgrd.50696.

Yang, K., T. Watanabe, T. Koike, X. Li, H. Fujii, K. Tamagawa, Y. Ma, and H. Ishikawa (2007), Auto-calibration system developed to assimilate AMSR-E data into a land surface model for estimating soil moisture and the surface energy budget, *J. Meteorol. Soc. Jpn.*, *85A*, 229–242.

Yang, K., T. Koike, I. Kaihotsu, and J. Qin (2009), Validation of a dual-pass microwave land data assimilation system for estimating surface soil moisture in semiarid regions, *J. Hydrometeorol.*, *10*, 780–793, doi:10.1175/2008JHM1065.1.

Yang, Z.-L., et al. (2011), The community Noah land surface model with multiparameterization options (Noah-MP): 2. Evaluation over global river basins, *J. Geophys. Res.*, *116*, D12110, doi:10.1029/2010JD015140.

Yuan, X., and E. F. Wood (2013), Multimodel seasonal forecasting of global drought onset, *Geophys. Res. Lett.*, *40*, 4900–4905, doi:10.1002/grl.50949.

Zaitchik, B. F., J. A. Santanello, S. V. Kumar, and C. D. Peters-Lidard (2013), Representation of soil moisture feedbacks during drought in NASA Unified WRF (NU-WRF), *J. Hydrometerol.*, *14*, 360–367.

Zhang, Y.-F., T. J. Hoar, Z.-L. Yang, J. L. Anderson, A. M. Toure, and M. Rodell (2014), Assimilation of MODIS snow cover through the Data Assimilation Research Testbed and the Community Land Model version 4, *J. Geophys. Res. Atmos.*, *119*, 7091–7103, doi:10.1002/2013JD021329.